Experiments in Fluids 30 (2001) 500–510 © Springer-Verlag 2001

Accelerations in water waves by extended particle image velocimetry

A. Jensen, J. K. Sveen, J. Grue, J.-B. Richon, C. Gray

Abstract Particle image velocimetry (PIV) measures instantaneous velocity across an extended area of flow by recording the motion of tracers suspended in and moving with the fluid. This principle is extended to the measurement of higher moments of the velocity field (acceleration) by recording the velocity field at two separate time instants using two cameras, viewing the same region of flow. Planar illumination of large areas within a hydrodynamic flow is achieved using a scanned argon ion laser beam and individual velocity measurements are made by cross-correlating image pairs acquired with a cooled, frame-straddling camera. A high-speed acousto-optic modulator is used to shut off the CW laser after two scans of the flow have been captured by the first camera. The modulator switches the beam back on for the second velocity measurement after a programmed delay. Synchronization of the cameras and beam modulator with the scanning beam system is achieved with a purpose-built multi-channel synchronizer device and operated from an integrated modular tree-based acquisition and processing software system. The extended PIV system is employed to measure the velocities and accelerations in periodic waves in a precise laboratory wave tank. A complementary theoretical description of Stokes waves provides a comparison with the measurements. The theoretical model is very precise, with an error term being less than 0.5% relative to the primary wave for the conditions of the experiments. The purpose is to test the measurement system and to judge the accuracy of the wave experiments under realistic and controllable conditions in the laboratory. Good agreement between the experiments and theory is found. The relative accuracy of the present experiments and measurements may be quantified in terms of the standard deviation due to an ensemble of measurements. In the best case, we find a relative standard deviation of 0.6% for the velocity measurements and 2% for the accelerations. It is indicated that such an accuracy may be generally achieved by appropriately choosing the size of the field of view.

1
Introduction

The rapid development of computers and advanced experimental tools has made it possible to perform investigations one earlier only could dream of. Today, almost every fluid mechanicist employs computers to complement theoretical studies and to analyse the equations of fluid flow for an increasingly wide range of applications. Less attention is perhaps paid to the considerable potential of an interplay between theoretical modelling and precise laboratory experiments. The recent advances of experimental techniques like particle image velocimetry (PIV) provide, however, both desired and attractive supplements to theoretical and computational investigations of complex problems in fluid mechanics. Precise experiments and advanced computation models developed in parallel may contribute to a better understanding of the physical problem and to a more robust modelling of the phenomenon under consideration. Precise experiments may also provide understanding of the inherent physics of new problems where simulation models are not successful. In the present paper, we shall describe a particle imaging system designed with the purpose to complement theoretical analysis. More precisely, we shall describe an extended particle imaging system, which can be used to measure not only the velocity field of the fluid, but also the accelerations. The ultimate goal has been to develop a system giving measurements, with sufficiently high precision, that could be used as input to theoretical modelling of various complex flows.

The acceleration field is calculated from the difference between two consecutive velocity fields. The latter are measured using directionally resolved digital particle image velocimetry (DPIV). The system uses two separate cameras viewing the same region of flow to acquire PIV images with no limitation on the time between individual velocity measurements. Both cameras record the same field of view with a small angle between their respective viewing axes. Precise alignment between the two fields is achieved using cross-correlation analysis similar to that used to extract the velocity field from image pairs acquired from individual cameras. Alternatively, one can use a dual

---

Received: 30 August 1999/Accepted: 30 August 2000

A. Jensen, J. K. Sveen, J. Grue (✉)
Mechanics Division, Department of Mathematics
University of Oslo, Norway

J.-B. Richon, C. Gray
Optical Flow Systems, Scotland

This work was conducted under the Strategic University Programme ‘General Analysis of Realistic Ocean Waves’ funded by the Research Council of Norway. The discussions with Dr. Didier Clamond, who also assisted with the data analysis leading to Fig. 6, and the technical assistance by Mr. Arve Kvalheim and Mr. Svein Vesterby are gratefully acknowledged.

camera system with beam-combining optics (or a multi CCD array camera), but the technical setup outlined in this paper is in general more flexible as it is easily extendable to 3D PIV measurements and combined PIV and laser induced fluorescence (LIF) measurements.

The acceleration measurement system is applied to water waves in a two-dimensional wave tank. The system is designed to cope with large measurement areas, typically up to 50 cm wide and high. To achieve this, a continuous wave argon ion laser coupled to a scanning beam system is used for illumination: this arrangement is particularly well suited to providing a large light sheet of uniform intensity. In addition, an acousto-optical cell modulates the light sheet such that only one laser scan is recorded on each image acquired by the CCD cameras. Synchronization between the system components is achieved with a programmable multi-channel synchronizer. Overall configuration, control, acquisition and analysis are performed from PIV software incorporating an integrated data management and logging system.

For the validation of our method, we measure accelerations in incoming Stokes waves in both deep water and finite depth. Waves are generated by a piston-type wave maker at one end of the tank and are absorbed by a beach at the other end. The measurements are performed for periodic progressive waves with wave slope up to 0.16. The measurements are compared with Stokes wave theory in deep water and for finite water depth. We generally find excellent agreement between experiments and theory. In the case of deep water, the theoretical model is valid up to the third order in the wave slope, giving an error term less than 0.5% relative to the primary wave. The theory is thus very precise. Previous measurements of acceleration in water waves have been performed by Jacobsen et al. (1997) and Chang and Liu (1998) and we compare our measurements with theirs (Sect. 4.2).

This paper is organized as follows. Section 2 describes the technical aspects of the system. The experiments are described in Sect. 3, together with the wave theory. Section 4 shows results compared with theory and Sect. 5 contains a conclusion.

2
Technical description of the PIV system

The acceleration measurements presented here are based on pairs of PIV measurements, and thus measures the change in velocity over a known time period. The system uses two separate cameras, each viewing the same region of flow and each recording an image pair for PIV evaluation. The acceleration field is calculated from the difference between two consecutive velocity fields. We use a standard (digital) cross-correlation PIV technique. The system consists of an illumination part, two cameras, a synchronizer and PC software.

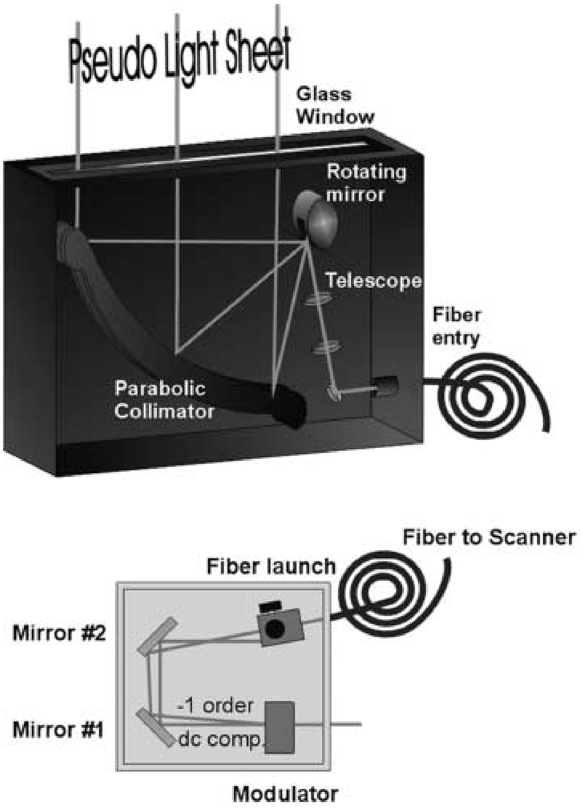

Fig. 1. The scanning beam system and acousto-optic-modulator (AOM)

2.1
Illumination

Following the need for two PIV measurements, a minimum of four light pulses are required for our acceleration measurements. One method for generating these pulses is to use a scanning beam system as described by Gray et al. (1991) and shown in Fig. 1. In this case a continuous-wave (CW) laser beam is collimated or slightly converging. This is deflected from an octagonal mirror to create a beam that repeatedly scans through 90 degrees. A parabolic mirror deflects and collimates the divergent pseudo light sheet into the flow area. This gives a stroboscopically pulsing light sheet that may be further modulated by shuttering the main CW beam with an acousto-optic modulator (AOM). The AOM is used to select two or more pulses for PIV recording. The light sheet formed with a CW laser and scanner is of very uniform intensity and well suited to PIV over large areas. The laser source is a Coherent Innova 300 argon ion laser emitting at all lines (488–514 nm), with a maximum continuous power output of 10 W. The beam is passed through an AOM crystal prior to being launched into a multi-mode optical fibre for delivery across the lab to the scanner positioned below the glass bed of the wave flume. The AOM crystal is driven by an RF amplifier which is switched on and off by a logic input. In the off state, the beam is transmitted directly through the AOM with very little attenuation of intensity (less than 4%). In the on state, the crystal medium is excited by a piezo-transducer; it then behaves like a diffraction grating. As the beam goes through the crystal, it is deviated by a known angle, which is a constant of the AOM crystal design. The launch optics of the fibre-optic link is positioned in such a way that the beam can be transmitted through the fibre only when it is deviated through the AOM. The combination of the AOM and the positioned fibre launch optics acts as a beam modulator with a response time of less than 1 µs. The output of the fibre-optic link is connected to the scanner via a lockable collet. The collimated beam is passed through a telescope arrangement that provides adjustment of the light sheet thickness by varying the position of the beam waist. The output of the scanner is a 50-cm-wide pseudo light sheet.

We note that the most common laser choice for PIV is a double-cavity Nd: YAG with beam-combining optics. The main benefit of this system is the flexibility of the pulse separations afforded by the use of two independent cavities and independence of pulse energy from pulse separation (compared with CW laser PIV). The main problem with the pulsed-laser arrangement in the general case of acceleration measurement, however, is the need for a minimum of four pulses per measurement. This requires four laser cavities and beam-combining optics for four beams. This kind of system does exist, but is extremely expensive. Additionally, light sheets formed with cylindrical optics will tend to be non-uniform in thickness and intensity, especially when used over a large measurement area.

2.2
Camera system

The system used here is an extension of a standard PIV configuration, using two separate cameras pointing to the same field of view with a small angle between them. The organization of its main components is shown in Fig. 2.

The two cameras used for image acquisition are high-sensitivity PCO Sensicam CCD cameras with a resolution of 1280 × 1024 pixels, and 12-bit digital outputs. To minimize noise and take full advantage of the available 12-bit dynamic range, the interline transfer CCD sensors are cooled to −15 °C and have a relatively low pixel readout rate. Images are transmitted to a host PC for storage and processing via high-speed digital fibre-optic link and a PCI frame grabber.

The cameras are used in dual-image mode: on reception of a control trigger, a first frame is exposed, then stored in on-chip registers and read out while a second image is being exposed. With this mode of operation, very short inter-image times, down to 200 ns, can be achieved when capturing an image pair. The "frame-straddling" technique takes direct advantage of this feature to acquire PIV image pairs.

One characteristic of operating the cameras in dual-image mode is that the exposure time of the first frame is controllable. When a scanning beam system is used, this first exposure can be accurately controlled such that the time and duration of the first frame records a single scan.

The exposure time of the second frame is fixed, however. This is determined by the CCD readout time of approximately 100 ms. The fixed-length exposure would record more than one scan depending on the scan rate used. This limitation is overcome by gating the laser beam with an AOM such that the beam is switched off after the first scan of the second frame.

The beam is then switched on again for the subsequent exposure of images on the second camera, implying that these exposures may also be contained in the second image of the first camera (depending on the time separations used). The main effect of this double exposure is that bright areas of the field of view tend to be brighter on the double-exposed image, thus leading in some cases to an increased number of false velocity vectors in these areas.

2.2.1
Synchronization

In an image acquisition sequence, consecutive scans of the flow field are recorded onto two consecutive frames of a frame-straddling CCD camera. This requires each camera to be externally triggered. The delay and duration of the trigger control pulse determines the delay and duration of the image 1 exposure on each camera. The camera control pulses are generated by the system synchronizer, which receives a synchronization pulse from the scanner at every scan of the flow field (see system diagram). The synchro-

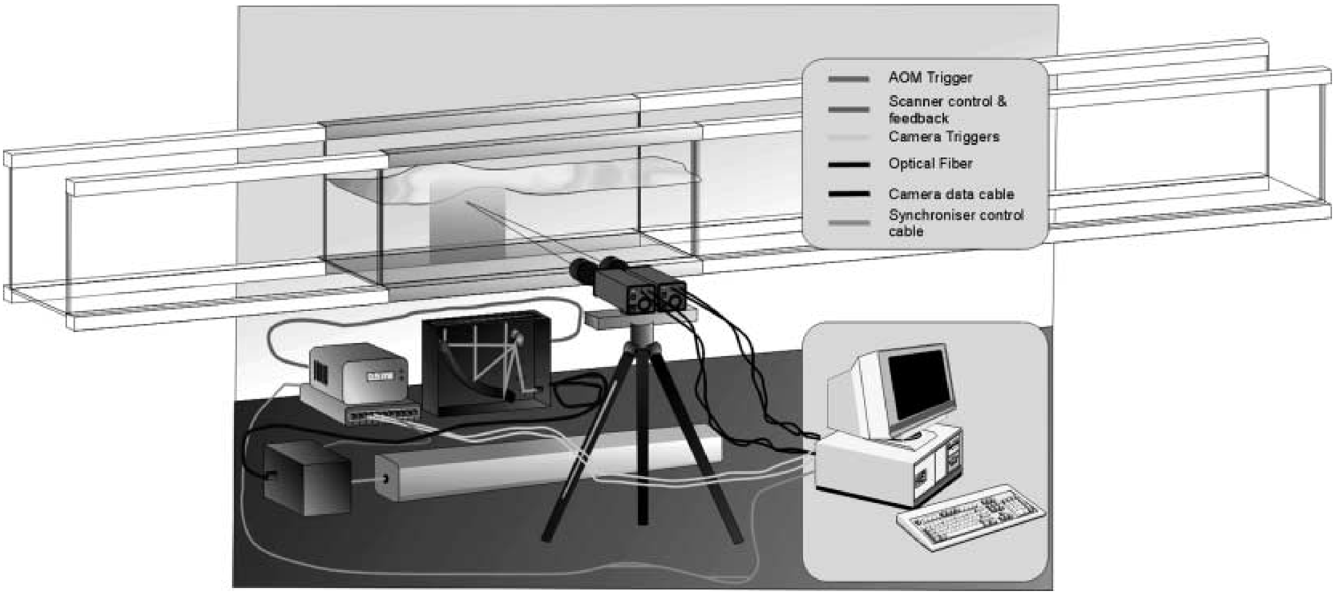

Fig. 2. Schematic drawing of experimental setup

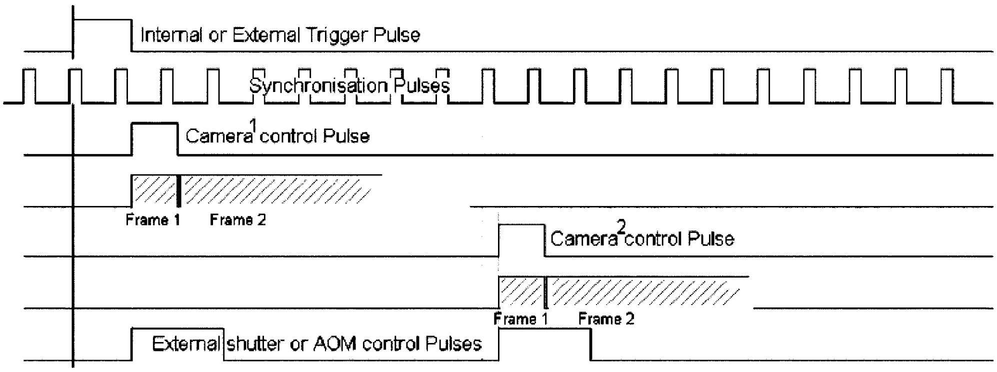

Fig. 3. Timing diagram

nizer measures the frequency and phase of the synchronization signal coming from the scanner and from this time base generates trigger pulses for camera 1, camera 2 and the acousto-optic modulator. A timing diagram describing the temporal relationship between the scanner synchronization signal, the camera and AOM triggers is given in Fig. 3.

An OFS TC412 synchronizer interfaces to the host PC through one of the COM ports and this is used by the system software for configuring the synchronization parameters as well as reading back the period of the synchronization signal.

The duration of the camera control pulses and the AOM control pulses are derived directly from the measured scanner frequency. The delay from the internal or external trigger to the camera or AOM control pulses also depends on the selected delay between camera acquisitions. The time separation between image pairs captured by camera 1 and 2, may be selected as an integer number of scan periods.

The external trigger input to the synchronizer may be used when an acquisition event is to be triggered by some external input, coming, for example, from a wave maker. Internal triggering is also possible where a sequence of acquisitions may be initiated at a range of frequencies up to the maximum frame rate of the camera (8 frames/s).

2.2.2
Alignment of the cameras

The two cameras are set up with the same field of view by simply positioning them side by side and rotated by an angle of 4.4°, so they both view the same region from slightly different perspectives.

The motion to be studied with the acceleration system is strongly two-dimensional. Thus, the images recorded at or near to 90° to the plane of the light sheet give closely representative values of the in-plane components of velocity. For simplicity and to maximize the effectiveness of the available light, a side-by-side camera arrangement is used. Alternatively, one could use a beam splitter in front of the cameras so that they view exactly the same region, but this would also reduce the light intensity on each image by 50%. Furthermore, the two-camera system is easily extendable to stereoscopic PIV for 3D measurements.

Initially, the two cameras are orientated so that the two fields of view align visually. This is done by viewing images of registration marks on a perspex sheet placed in the tank at the plane of the light sheet. The cameras are first orientated perpendicular to the wall of the tank by focusing the cameras on the glass outer surface of the tank. The orientation of the cameras is then adjusted so that the image of each camera reflected on the tank wall is exactly in the centre of the respective images. The focus of the cameras is then adjusted back to the plane of the light sheet and the cameras are tilted towards each other in the horizontal plane by the same amount until the images are roughly aligned according to the registration marks. The perspex sheet is then removed and the water in the tank seeded. The camera orientation is then fine-tuned by cross-correlating the base image of camera 1 with the base image of camera 2 in the same way as standard cross-correlation is used for measuring particle displacements. The vector maps produced in this way give a direct measure of the misalignment. Using on-line cross-correlation analysis alignment can be performed quite quickly and to within 2–3 pixels across the whole field of view.

Acceleration is derived from the difference between velocity measurements made from two separate and slightly different perspectives, at different time instants. It is therefore important to consider what effect the difference in perspective has on the acceleration measurements in the case of this application.

A test was carried out recording the velocity field due to the waves we discuss in Sect. 3 (Figs. 5–8, with $a = 2.05$ cm and $\omega = 8.95\ \mathrm{s}^{-1}$). But, instead of triggering the cameras with a small time difference between them, the cameras were triggered simultaneously. The images thus acquired were then analysed and the vector fields compared. Because the cameras were triggered simultaneously, the difference between the two vector maps give a measure of the effect of viewing the flow from slightly different perspectives. This effect could have been estimated from geometrical considerations, but this direct method also accounts for other factors such as viewing through the wave tank walls and lens distortion. Images were taken with 12-ms separation and interrogated using 32 × 32 pixels large non-overlapping interrogation areas.

Table 1. Difference between vector fields as measured by two cameras

Angle	Minimum	Mean	Maximum	$\lvert\mathbf{d}_\mathrm{m}\rvert$
4.4°	0.00224 pixels	0.13 pixels	0.45 pixels	6.90 pixels
8.0°	0.0056 pixels	0.18 pixels	0.65 pixels	7.03 pixels

For the 4.4° camera separation, used for acceleration measurements, the difference between the instantaneous vector field measured from camera 1 and camera 2 is presented in Table 1. For comparison, an angle of 8° is also checked. As a reference, the table also includes the mean of the displacement field due to the waves, $|\mathbf{d_m}| = \sqrt{d_x^2 + d_y^2}$. We observe that the average error introduced by viewing the flow from slightly different angles is 1.9–2.6% relative to $|\mathbf{d_m}|$.

2.3
Acquisition and analysis software

Both the cameras and the synchronizer are interfaced to the host PC and are controlled from a single software package (VidPIV3-Rowan, Optical Flow Systems 1999). This is a complete control and analysis software tool, including a state-of-the-art graphical user interface.

On setting up the equipment for use in an experiment, the cameras are aligned to view the desired region of flow. Then, they are calibrated by generating a mapping from an acquired image of a grid with known points on it and referenced to a convenient origin. Acquired images are initially processed using cross-correlation on a grid specified in real units using the image mapping to transpose to pixel coordinates. The vector maps generated in this way are filtered using both global and local filtering and then interpolated.

Tests have also been performed with another PIV software (Sveen 1999), finding excellent agreement with both VidPIV measurements and theory (results not shown).

3
The experiments

We now apply the extended PIV system to measurements of velocities and accelerations due to periodic waves propagating in a wave tank. A complementary theoretical description of the waves provides a comparison with the measurements. The purpose is to test the PIV system and judge the accuracy of the wave experiments under realistic and controllable conditions in the laboratory. The wave tank is 24.6 m long, 0.5 m wide and filled with water to a depth of 0.6 m. In one end of the tank there is a hydraulic-piston wave maker with movements controlled by a computer. At the other end there is an absorbing beach to damp the waves. The position of the cameras is 12.5 m from the wave maker. The measurements are terminated before any small reflected waves from the beach appear at the recording position. The wave tank and the motion of the wave maker are very precise. The wave generation in the tank has previously been examined in detail: for Stokes waves (Huseby and Grue 2000) and for focusing wave groups (Jensen and Grue 1999), finding excellent agreement between experiments and theoretical models.

3.1
The incoming waves

A sinusoidal motion of the wave maker with frequency ω generates a wave train which has a transient leading part followed by waves which are periodic. We pay attention to the periodic part of the wave train, where the waves are characterized by the wave amplitude a, the frequency ω, the wave number k and the corresponding wave length λ. Most of the runs are performed with a wave length comparable to the depth h of the water. This means that the waves, to a good approximation, are deep-water waves. The surface elevation η of the periodic waves may be described by

$$\eta = a\cos(kx - \omega t) + a^{(2)}\cos 2(kx - \omega t) + a^{(3)}\cos 3(kx - \omega t) + \cdots \tag{1}$$

including the locked higher harmonic components with amplitudes $a^{(n)}$ ($n > 1$) accompanying the fundamental mode. In Eq. 1, the horizontal x-axis along the length-direction of the wave tank and the time t are introduced. The surface elevation is recorded by wire gauges at several places in the wave tank to document the incoming wave field. The wave amplitude is determined from the fundamental harmonic oscillation of η. The measurements of the higher harmonic waves follow Grue (1992) and show that $a^{(2)} \simeq (1/2)a^2k$, $a^{(3)} \simeq (3/8)\ a^3k^2$ and $a^{(n)} \simeq 0$ for $n > 3$ and $ak < 0.2$. This means that the incoming waves may be regarded as pure Stokes waves and that the fluid motion to a good approximation may be described by the velocity potential

$$\phi = \frac{ag}{\omega}\exp(ky)\sin(kx - \omega t) + \mathcal{O}(a^4)\ . \tag{2}$$

In Eq. 2, $\omega^2 = gk(1 + a^2k^2)$, g denotes the acceleration due to gravity, and the vertical y-axis is pointing upwards, with $y = 0$ in the mean free surface. The relation (Eq. 2) is a simple high-order approximation of the velocity potential, see, for example, Newman (1977, §6.4). We note that small parasitic second-harmonic waves are generated at the wave maker propagating at half the speed of the wave field (1)–(2). These waves arrive at a late time at the recording position, and we terminate the measurements before the parasitic waves appear.

Some of the experiments are performed when the effect of a finite water depth is essential. In this case, the fluid motion is governed by the potential

$$\phi = \frac{ag}{\omega}\frac{\cosh k(y+h)}{\cosh kh}\sin(kx - \omega t) + \mathcal{O}(a^2)\ , \tag{3}$$

where $\omega^2 = gk\tanh kh(1 + f(kh)\cdot(a^2k^2))$ and $f(kh)$ is a function of kh, given in, for example, Mei (1989, §12.3).

3.2
Recording the images and filtering

As previously noted, sequences of two image pairs are captured for the subsequent analysis of the velocity and acceleration fields of the waves. Each sequence is triggered by the computer that controls the wave maker. The triggering is very accurate and has a variability of less than the scanner period of the PIV system (set to 12 ms in most of the experiments and to 8 ms in a few runs). This level of precision is important since several repetitions with the same wave conditions are performed, capturing different phases of the wave. The water in the tank is seeded with conifer pollen with diameter approximately 70 μm. The field of view is 23 cm × 18 cm in all the runs. In most experiments an interrogation window of 32 × 32 pixels with an overlap of 50% is used. In some experiments the interrogation window was 64 × 64 pixels (results not shown). When the cross-correlation analysis is finished the raw velocity vectors are validated with a global window velocity filter that allows selection of velocity limits $V_x$min, $V_x$max, $V_y$min and $V_y$max. The filter creates a scatter plot and shows the distribution of velocities in the vector map. From this plot typical values of the upper and the lower bounds of the velocity are chosen. This global filter will typically not identify outliers that are of the same magnitude as the surrounding flow, and we therefore also apply a local median filter. This filter removes vectors that fall outside a limit $\mathbf{V}_{\mathrm{lim}}$ defined by

$$\mathbf{V}_{\mathrm{lim}} = \mathbf{V}_{\mathrm{median}} \pm F \times \mathbf{V}_{\mathrm{std}} \quad , \tag{4}$$

where $F = 1.5$ and $\mathbf{V}_{\mathrm{median}}$ and $\mathbf{V}_{\mathrm{std}}$ is the median and standard deviation, respectively, of the eight surrounding neighbours to a vector $\mathbf{V}(i, j)$. Finally identified outliers are interpolated by a 3 × 3 kernel with a weighted mean technique, following Wang et al. (1996).

4
Results

Two different wave frequencies are used to obtain the results shown below. Experiments with other frequencies are also performed obtaining similar results (not shown). In the first set, the wave frequency is $\omega = 8.95\ \mathrm{s}^{-1}$ and the amplitude measured by wire gauges is $a = 2.05$ cm. The wave number estimated from the dispersion relation is $k = 7.95\ \mathrm{m}^{-1}$ giving $\lambda = 0.79$ m and a wave slope of $ak = 0.16$. The magnitudes of the fluid velocity and the acceleration are $0.17\ \mathrm{ms}^{-1}$ and $1.6\ \mathrm{ms}^{-2}$, respectively, at the mean free surface.

The output of the PIV evaluations are the two velocity fields $\mathbf{v}(\mathbf{x}, t_1)$ and $\mathbf{v}(\mathbf{x}, t_2)$ at the two time instants t_1 and t_2, respectively. In most of the experiments, the time separation between images 1 and 2 and between images 3 and 4 is 12 ms, while t_2–t_1 is 60 ms. In Fig. 10, the corresponding intervals are 8 ms and 64 ms. Examples of $\mathbf{v}(\mathbf{x}, t_1)$ and $\mathbf{v}(\mathbf{x}, t_2)$ are visualized in Fig. 4. We note that the velocity field at time t_1 contains some spurious vectors near the surface of the fluid. This is because the second image of camera 1 (image 2 in the sequence) contains the images 3 and 4, since the shutter of camera 1 is open during the exposure of camera 2. The result is that the free surface in image 2 becomes relatively thick and extraction of velocity vectors for $\mathbf{v}(\mathbf{x}, t_1)$ close to the free surface becomes more uncertain than inside the fluid domain. The fact that image 2 contains images 3 and 4 also means that the time separation t_2–t_1 should be much greater than the scan period, to avoid correlation between image 1 and images 3–4.

The acceleration field $\partial\mathbf{v}/\partial t$ may be estimated by evaluating

$$\frac{\mathbf{v}(\mathbf{x}, t_2) - \mathbf{v}(\mathbf{x}, t_1)}{t_2 - t_1} \quad . \tag{5}$$

Figure 5 shows an example of the acceleration field as calculated from the velocity fields shown in Fig. 4.

The measured velocity and acceleration fields may be compared with the corresponding fields due to the theoretical Stokes waves determined by Eq. 2. The latter predicts an exponential decay in the vertical direction according to $\exp(ky)$ of the velocities and the accelerations, with k determined from the dispersion relation. It is tempting to fit the measured quantities with this exponential profile. Results obtained by a least squares minimization show that the measurements are very close to the fitted curves. Examples are displayed in Fig. 6.

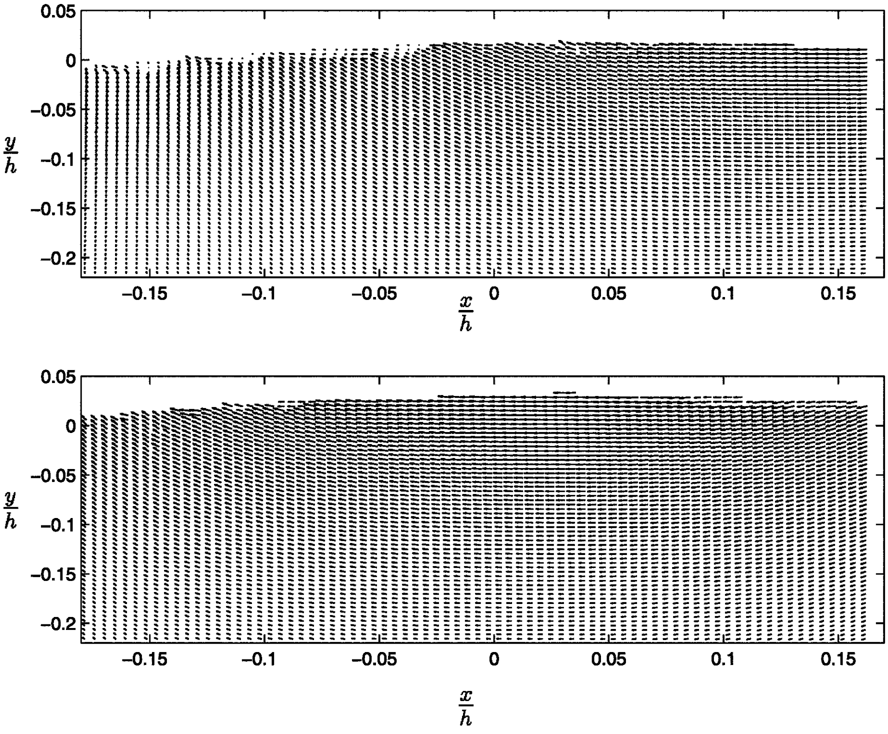

Fig. 4. Velocity fields. Waves with $\omega = 8.95\ \mathrm{s}^{-1}$, $ak = 0.16$ and $kh = 4.9$. Top: $\mathbf{v}(\mathbf{x}, t_1)$. Bottom: $\mathbf{v}(\mathbf{x}, t_2)$

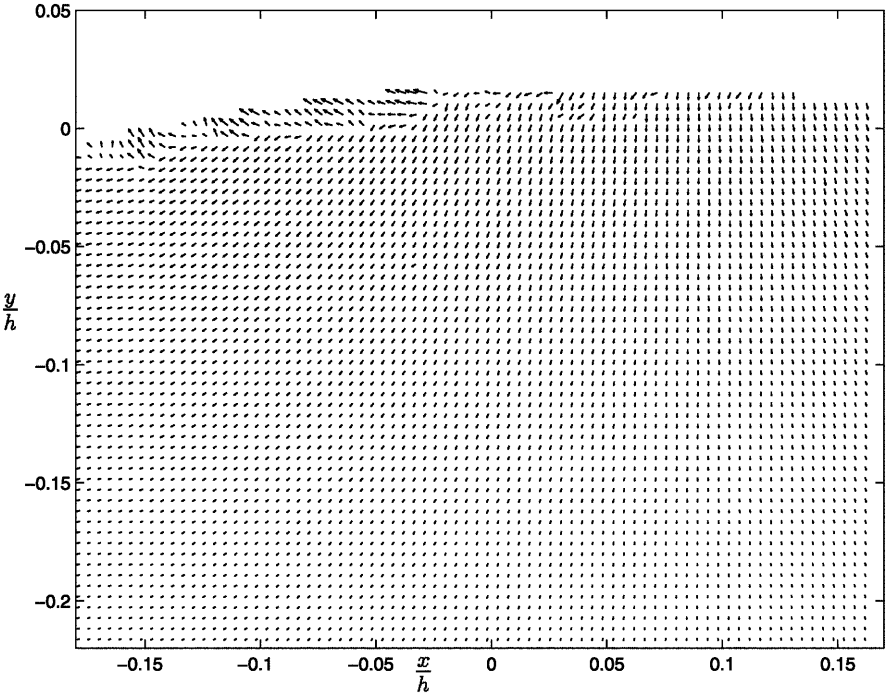

Fig. 5. Acceleration field, $(\mathbf{v}(\mathbf{x},\ t_2) - \mathbf{v}(\mathbf{x},\ t_1))/t_2 - t_1$

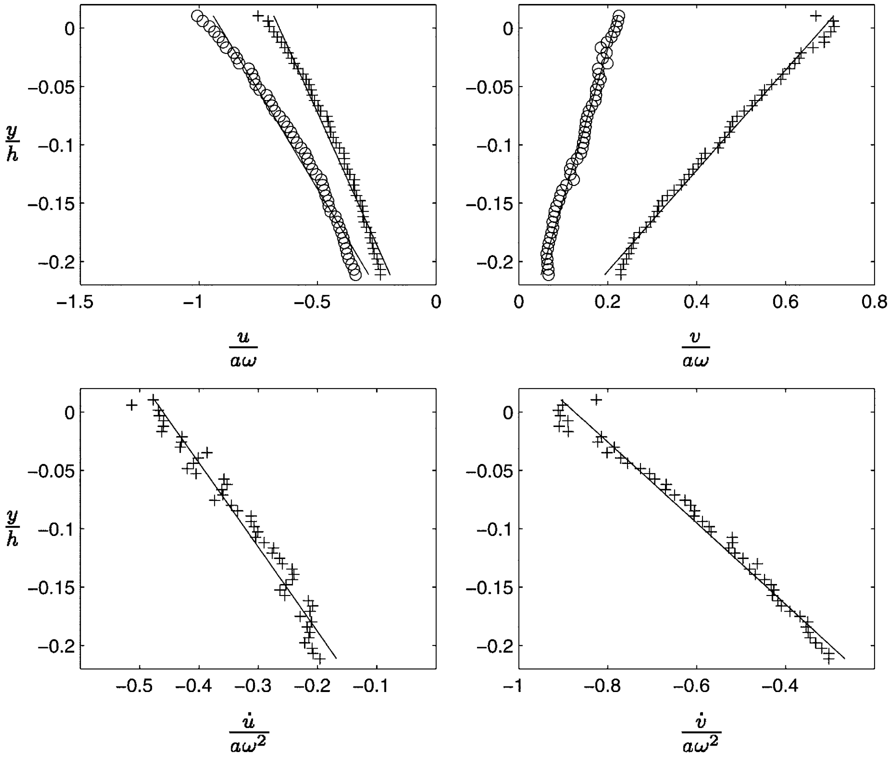

Fig. 6. Velocity and acceleration measurements. $\omega = 8.95\ \mathrm{s}^{-1}$, $ak = 0.16$, $kh = 4.9$. Solid line theory. *Top left*: '+' and 'o' experimental velocity profiles $u(\mathbf{x}, t_1)$ and $u(\mathbf{x}, t_2)$, respectively, x-position fixed. *Top right*: same as the left figure except that this contains the vertical velocity profiles $v(\mathbf{x}, t_1)$ and $v(\mathbf{x}, t_2)$. *Bottom left*: '+' horizontal acceleration profile $(u(\mathbf{x}, t_2)–u(\mathbf{x}, t_1))/(t_2–t_1)$. *Bottom right*: '+' vertical acceleration profile $(v(\mathbf{x}, t_2)–v(\mathbf{x}, t_1))/(t_2–t_1)$

For further comparison of the experiments with the theory, we may exploit that the magnitude of $\mathbf{v}$ and $\partial\mathbf{v}/\partial t$ of the Stokes waves (Eq. 2) are independent of the horizontal coordinate (x). We thus derive

$$\alpha \equiv \frac{\omega|\mathbf{v}|}{agk} = \frac{\omega}{agk}[u^2 + v^2]^{\frac{1}{2}} = \exp(ky)\ , \qquad (6)$$

$$\dot{\alpha} \equiv \frac{|\partial\mathbf{v}/\partial t|}{agk} = \frac{1}{agk}\left[u_t^2 + v_t^2\right]^{\frac{1}{2}} = \exp(ky)\ , \qquad (7)$$

where $(u, v) = \mathbf{v}$ and $(u_t, v_t) = \partial\mathbf{v}/\partial t$. We may check how close the measured α and $\dot{\alpha}$ are to the theoretical counterpart $\exp(ky)$. In Fig. 7, we have plotted α and $\dot{\alpha}$ due to the measurements in Figs. 5–6 as function of the vertical coordinate (y). Four horizontal positions are selected: $x/h = -0.15, -0.5, 0.5, 0.15$. We observe that the measurements are very close to the theoretical prediction for every abscissa. The results in Fig. 7 for $x/h = 0.05, 0.15$ are particularly good.

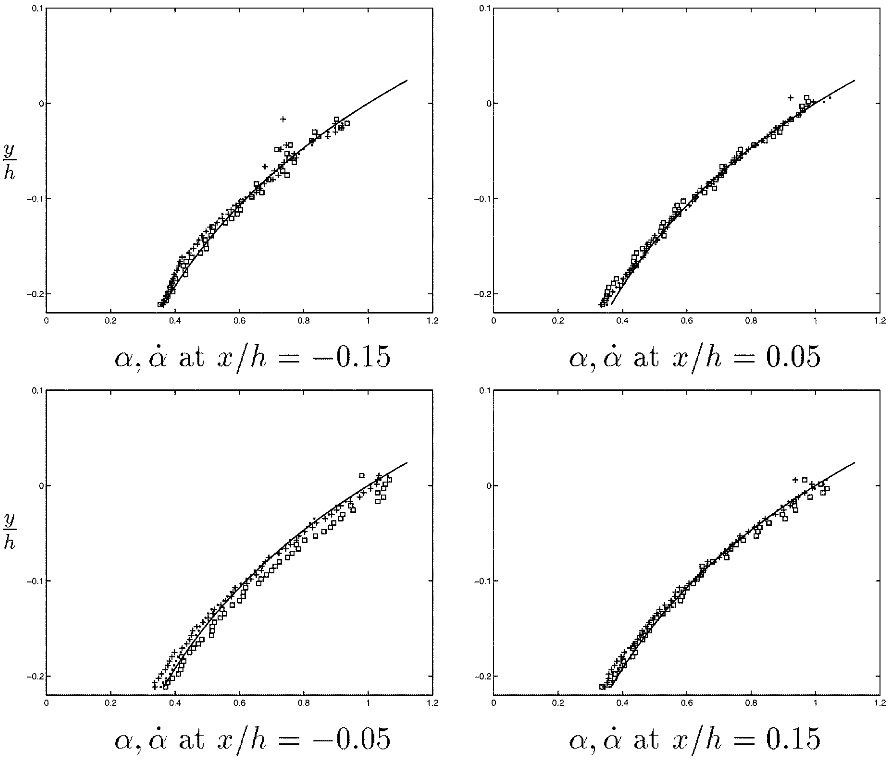

Fig. 7. Velocity and acceleration measurements. $\omega = 8.95\ s^{-1}$, $ak = 0.16$, $kh = 4.9$. '.' $\alpha(y)$ for $t = t_1$, '+' $\alpha(y)$ for $t = t_2$ and *squares* are $\dot{\alpha}(y)$. *Top left*: $\alpha(y)$ and $\dot{\alpha}(y)$ for $x/h = -0.15$. *Bottom left*: same as above except $x/h = -0.05$. *Top right*: $x/h = 0.05$. *Bottom right*: $x/h = 0.15$. α and $\dot{\alpha}(y)$ defined in the text. Solid line $\exp(ky)$

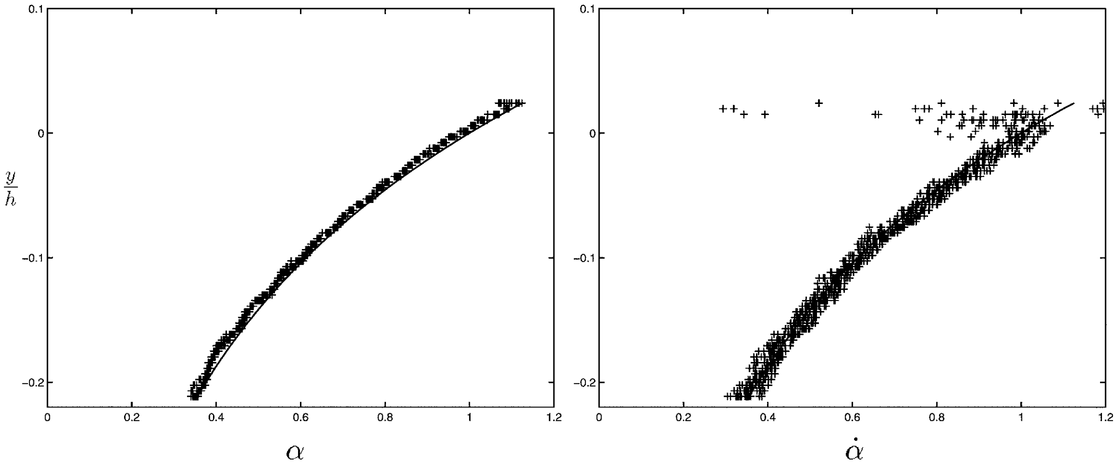

Fig. 8. Velocity and acceleration measurements, $\omega = 8.95\ \mathrm{s}^{-1}$, $ak = 0.16$ and $kh = 4.9$. *Left*: '+' are 20 columns of velocity measurements taken from the velocity field of the crest. *Right*: same as the left except that this is acceleration measurements (25 columns). α and $\dot{\alpha}(y)$ defined in the text. Solid line $\exp(ky)$

Repeated tests are performed capturing different phases of the waves. The measured results always exhibit velocity and acceleration profiles close to the theory (Eqs. 2, 6, 7) with some minor scatter. We note that the phase of the wave does not contribute to α and $\dot{\alpha}$, according to theory. This means that typical scatter of the measurements may be visualized by comparing these quantities for several columns of the velocity and acceleration maps. Results in Fig. 8 show α and $\dot{\alpha}$ for 20–25 columns of Figs. 5–6 near the crest of the wave. The experimental results fit well with the theoretical profile $\exp(ky)$ apart from some minor scatter. The scatter is somewhat larger for the accelerations than for the velocities.

To quantify the scatter, we evaluate the vertical average of the row-wise standard deviation of α and $\dot{\alpha}$. More specifically we evaluate

$$\sigma = \frac{1}{M}\sum_{m=1}^{M}\left(\frac{1}{N}\sum_{n=1}^{N}\left(V(m,n) - \bar{V}(m)\right)^2\right)^{1/2} \tag{8}$$

where V is either α or $\dot{\alpha}$, M and N denote the number rows and columns of the velocity and acceleration maps, respectively, and $\bar{V}$ the row-wise mean given by

$$\bar{V}(m) = \frac{1}{N}\sum_{n=1}^{N} V(m,n) \ . \tag{9}$$

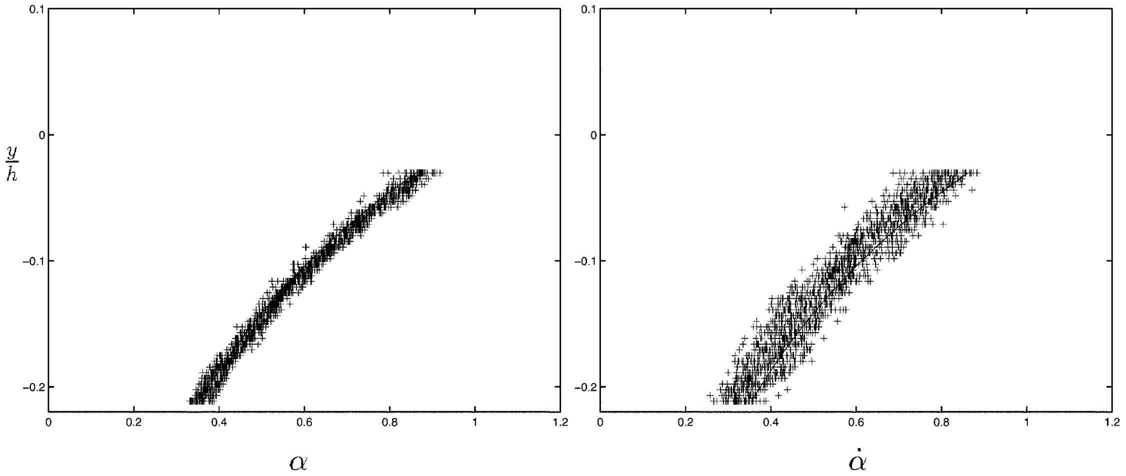

Fig. 9. Same as Fig. 8, but $ak = 0.09$, 40 columns

The value of σ determined by Eq. 8 is 0.6% (relative to unity) for the velocities and 2% for the accelerations shown in Fig 5. These results are due to 40 columns. Obviously, eventual small variations in the experimental wave field contribute to these digits.

Experiments are also performed with a smaller wave amplitude of $a = 1.2$ cm with $ak = 0.09$ keeping the wave frequency $\omega = 8.95\ \mathrm{s}^{-1}$. In this case, typical velocities and accelerations at the free surface are 0.11 ms^{-1} and 0.96 ms^{-2}, respectively. Results for 40 columns of the velocities and accelerations are shown in Fig. 9. The results fit quite well with the theoretical curve $\exp(ky)$. There is, however, a larger scatter in the results for the smaller wave amplitude than for the larger. The value of σ determined by Eq. 8 is 3% for the velocities and 7% for the accelerations shown in Fig. 9. These results illustrate that the relative accuracy becomes poorer when the wave amplitude and thereby the fluid velocity is reduced. Conversely, the relative accuracy is improved when the wave amplitude is increased. This also illustrates that high accuracy may be achieved by appropriately choosing the size of the field of view.

We have also done some experiments with relatively long waves, with $\omega = 3.77\ \mathrm{s}^{-1}$ and $a = 7.5$ cm ($ak = 0.14$). In this case, the magnitude of the fluid velocity at the mean free surface is 0.36 ms^{-1} while the fluid acceleration is 1.4 ms^{-2}. Furthermore, $\lambda = 3.46$ m and $kh = 1.09$, thus the effect of a finite depth has to be taken into account. From Eq. 3 we may derive

$$\beta \equiv \frac{\omega \cosh kh}{agk}\left[\frac{u^2}{\cosh^2 k(y+h)} + \frac{v^2}{\sinh^2 k(y+h)}\right]^{\frac{1}{2}} = 1 \ , \tag{10}$$

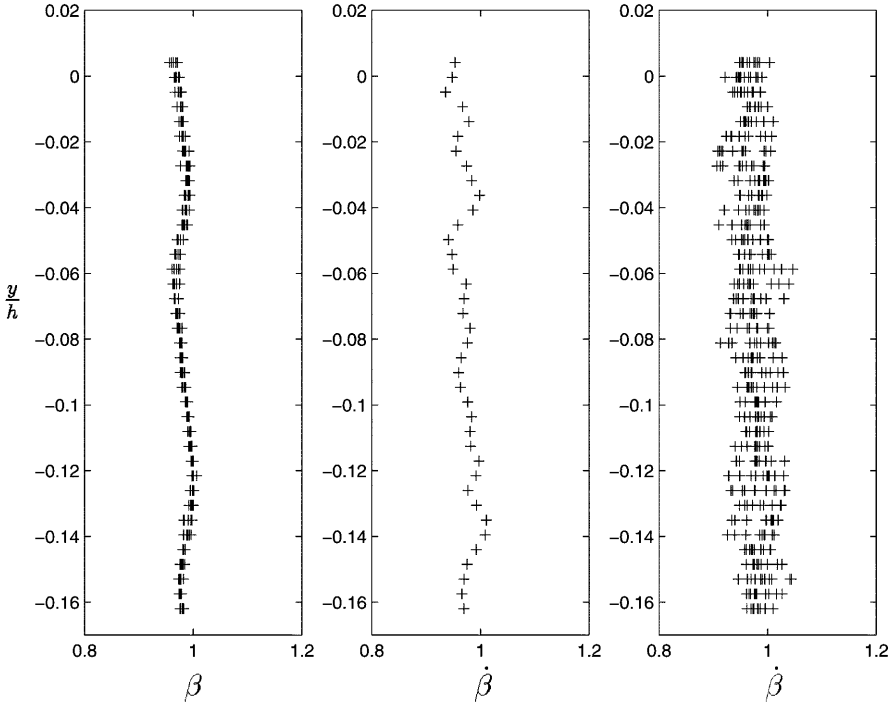

Fig. 10. Velocity and acceleration measurements, $\omega = 3.77\ \mathrm{s}^{-1}$, $ak = 0.14$ and $kh = 1.09$. *Left*: '+' are 5 columns of velocity measurements taken from the velocity field. *Middle*: acceleration measurements, one column. *Right*: acceleration measurements, 10 columns. β and $\dot{\beta}$ are defined in the text

$$\dot{\beta} \equiv \frac{\cosh kh}{agk}\left[\frac{u_t^2}{\cosh^2 k(y+h)} + \frac{v_t^2}{\sinh^2 k(y+h)}\right]^{\frac{1}{2}} = 1 \ . \tag{11}$$

In Fig. 10 we have plotted the measured β and $\dot{\beta}$. The scanner period is now 8 ms while t_2–$t_1 = 64$ ms. The measurements are rather close to the theory. The value of σ due to 40 columns determined by Eq. 8 is 3% for the velocities and 7% for the accelerations.

4.1
Error sources

The results are disturbed by errors from several different sources, including an error due to misalignment of the cameras. The latter is true for the acceleration measurements (but not for the velocity). The misalignment introduces a constant small shift, $\Delta_1\mathbf{v}$, between the consecutive velocity fields leading to an error of the normalized acceleration given by

$$\frac{1}{agk}\frac{\Delta_1\mathbf{v}}{\Delta t} \simeq \frac{\Delta_1\mathbf{v}}{a\omega}\frac{1}{\omega\Delta t} \ . \tag{12}$$

While $\omega\Delta t = 0.5$ in the experiments (Figs. 5–9), $|\Delta_1\mathbf{v}/a\omega|$ is from the results in Sect. 2.2.2 (Table 1) estimated to be 0.019–0.026. We then evaluate

$$\epsilon_p = \frac{1}{M}\sum_{m=1}^{M}\left(\frac{1}{N}\sum_{n=1}^{N}\dot{\alpha}(m,n) - \exp(ky(m))\right) \ , \tag{13}$$

finding that $\epsilon_p = 0.02$ for the results presented in Fig. 8b and 0.03 for the results in Fig. 9b. These values are comparable to the error one should expect due to misalignment. (The corresponding values for α are 0.01 and 0.015, respectively). An error introduced by misalignment between the cameras does not affect the value of the standard deviation of the measurements of $\dot{\alpha}$ as defined in Eq. 8.

On this point, we should keep in mind that the measured velocities and accelerations are normalized by the wave amplitude. The latter is estimated by wire gauge recordings with a relative accuracy of 2–3%, which is of the same order of magnitude as the error discussed above.

We also note that an error due to finite differencing of the oscillatory velocity field reads

$$|1 + (i\omega\Delta t)/2| - 1 \cong 0.03 \tag{14}$$

(for $\omega\Delta t = 0.5$).

Errors in regular PIV measurements have been thouroughly covered in previous work, see, for example, Raffel et al. (1998) for an overview.

4.2
Comparison with other work

Documented acceleration measurements of water waves using PIV are few. Our results are compared with the previous investigations we have become aware of (Jakobsen et al. 1997; Chang and Liu 1998). In the former work, a system with a scanning laser beam system, a 15 W Ar-ion laser, one lens, four CCDs and beam splitters was employed to obtain a sequence of four images (images A, B, C, D), each receiving 25% of the light intensity of the beam. The resolution of the CCDs were 768 times 484 pixels. Accelerations in standing waves were obtained, with linear theory as theoretical reference. The data of the waves were: period 1 s ($\omega = 6.28$ s^{-1}), linear wave length 1.56 m, amplitude 60.7 mm, estimated wave slope 0.24. The scan rate was 5 ms and the time separation between frames B and C, as defined above, was 35 ms. Jakobsen et al. (1997) claim that correlation noise was visually present in the acceleration vector maps, introducing an uncertainty of 10–20% for the vertical acceleration and 50–100% for the horizontal acceleration. For small accelerations, noise could obscure the structures contained within a map presenting a single recording of the acceleration field. Spatially averaging reduced the error by a factor of 20–30, but then the spatial resolution of the acceleration field was lost. The accuracy of the acceleration field in their work is inferior compared to the results described here.

Jakobsen et al. (1997) also investigated waves breaking at a vertical wall and obtained the integrated pressure from acceleration measurements, but the acceleration field was not given in these experiments.

Chang and Liu (1998) estimated a spatially averaged Lagrangian acceleration in the tip of a breaking wave. They generated a laser sheet using a frequency double dual Nd: YAG. The CCD camera had a resolution of 1316 times 1034 pixels. The data of their wave tank experiments were: wave maker performing periodic oscillations in time with period 1 s ($\omega = 6.28$ s^{-1}) and amplitude 7 cm in water, with still water depth 20 cm. The generated waves broke at a distance of 38 cm from the wave paddle. The wave height recorded by a wave gauge prior to breaking was 14.5 cm and the linear wave length was 121 cm. Their time interval between two pulses was 2 ms, while the time between two consecutive velocity fields was 55 ms. They give only one acceleration estimate in their report; viz. the typical acceleration in the tip of the wave, which was 1.1 g. They applied a small field of view and tilted the camera significantly (45°) to obtain sufficient resolution close to the free surface. No error estimate of the acceleration was given. (The velocity field had an estimated error of the same order of magnitude as in our measurements.) Thus, it is not possible to directly compare their and our results.

It is evident, however, that our system may in an accurate way record the velocity and acceleration fields in steep and even breaking waves. Work on this topic is in progress, see Huseby et al. (2000), Jensen et al. (2000).

5
Conclusion

An extended PIV system to measure the accelerations $\partial\mathbf{v}/\partial t$ of a velocity field $\mathbf{v}$ of a fluid is described. The system consists of two CCD cameras, a scanning laser beam and a synchronizer controlled and monitored by a computer. The laser source is a CW argon ion laser, sufficiently powerful (10 W) to provide light for sequences of recorded image pairs. The two high-sensitive cooled PCO Sensicam cameras have a resolution of 1280 × 1024 pixels with 12-bit digital output.

A high-speed acousto-optic modulator is used to shut off the CW laser after two scans of the flow have been captured by the first camera. The modulator switches the beam back on for the second velocity measurement after a programmed delay. Synchronization of the cameras and beam modulator with the scanning beam system is achieved with a purpose-built multi-channel synchronizer device and operated from an integrated modular tree-based acquisition and processing software system.

The system is applied to measure the accelerations due to water waves in a wave tank of standard laboratory size. It is tested for several wave parameters in the laboratory. Results are displayed for waves with frequency $\omega = 8.95\ \mathrm{s}^{-1}$ and amplitude either 1.09 cm or 2.05 cm. In another set of experiments the frequency is $\omega = 3.77\ \mathrm{s}^{-1}$ and the amplitude is 7.5 cm. In all cases, the water depth is 0.6 m. The fluid velocity and the acceleration at the position of mean free surface are in the ranges 0.11–0.36 ms^{-1} and 0.96–1.6 ms^{-2}, respectively. The experiments are compared with theoretical Stokes waves. In the cases with wave frequency $\omega = 8.95\ \mathrm{s}^{-1}$, the waves are deep-water waves, practically speaking. The theoretical model is then valid up to the third order in the wave slope, giving an error term being less than 0.5% relative to the primary wave, for the conditions in the experiments. Thus, the theory is very precise.

With the cross-correlation technique used in the PIV analysis we get an absolute error of the velocity measurements which may not in practice be reduced beyond a certain value. The relative error is hence smaller for high-velocity flows than for small-velocity flows. This is confirmed by the experiments (Figs. 8–9). This means that a small relative error may generally be achieved by appropriately choosing the size of the field of view. The accelerations are found to be somewhat more noisy than the velocities since they are obtained by a finite difference method. Agreement between theory and experiment is satisfactory, however. The relative accuracy of the present experiments and measurements may be quantified in terms of the standard deviation due to an ensemble of measurements, determined here by Eq. 8. In the best case, we find a relative standard deviation of 0.6% for the velocity measurements and 2% for the accelerations. We thus conclude that our PIV system is efficient for velocity and acceleration measurements due to gravity waves.

We have also compared our measurements of accelerations in water waves with those of others. Chang and Liu (1998) measured velocities and accelerations in breaking waves. Their wave data were: frequency $\omega = 6.28\ \mathrm{s}^{-1}$, wave height 14.5 cm, typical velocity 2 ms^{-1}, maximal acceleration about 1.1 g, water depth 0.2 m, measurement position 0.35 m from the wave paddle. They commented that their PIV system gave rather good accuracy for the cases investigated, but no documentation was given. Another group, Jacobsen et al. (1997), measured the velocities and accelerations due to standing waves with frequency $\omega = 6.28\ \mathrm{s}^{-1}$ and amplitude 6.07 cm, finding good results for the velocities, but rather uncertain results for the acceleration field. It may be true that the novel high-resolution and high-sensitive extended PIV system outlined here and that by Chang and Liu, exploiting a different system from ours, provide significant technological improvements of previous techniques to measure accelerations in fluids. With the continuous development of camera technology, similar but more precise systems are expected to appear in the near future. We find, however, that the extended PIV system outlined here is quite suitable for investigations of various unresolved aspects of non-linear gravity waves, where work is in progress (see Huseby et al. 2000; Jensen et al. 2000).

We have considered the acceleration term $\partial \mathbf{v}/\partial t$. The complete acceleration is obtained by adding $\mathbf{v} \cdot \nabla \mathbf{v}$ which involves evaluation of $\nabla \mathbf{v}$. Fairly precise evaluation of the latter term my be obtained by numerical differentiation of the velocity field. (Examples for internal waves are found in Grue et al. 2000.) We finally note that the present two camera PIV system is easily extendable to 3D PIV measurements and combined PIV and LIF measurements.

References

Chang K-A; Liu PL-F (1998) Velocity, acceleration and vorticity under breaking waves. Phys Fluids 10: 327–329

Gray C; Greated CA; McCluskey DR; Easson WJ (1991) An analysis of the scanning beam PIV illumination system. Meas Sci Technol 2: 717–724

Grue J (1992) The nonlinear water waves at a submerged obstacle or bottom topography. J Fluid Mech 244: 455–476

Grue J; Jensen A; Rusas P-O; Sveen JK (2000) On the breaking and broadening of internal solitary waves propagating in stratified fluid. J Fluid Mech 413: 181–217

Huseby M; Grue J (2000) An experimental investigation of higher harmonic forces on a vertical cylinder. J Fluid Mech 414: 75–103

Huseby M; Jensen A; Grue J (2000) An experimental investigation of ringing loads on a vertical cylinder in transient waves. In: Miloh T, Zilman G (eds) Proceedings of the 15th International Workshop on Water Waves and Floating Bodies, Caesarea, Israel, 27 February–1 March, pp 75–78

Jakobsen ML; Dewhirst TP; Greated CA (1997) Particle image velocimetry for predictions of acceleration fields and force within fluid flows. Meas Sci Technol 8: 1502–1516

Jensen A; Grue J (1999) On the difference in the speed of gravity waves in a physical and numerical wave tank. Pre-Print. Dept. of Mathematics, University of Oslo, Oslo, Norway

Jensen A; Sveen JK; Huseby M; Grue J (2000) Measurements of velocities and accelerations in steep irregular water waves. 10th International Symposium on Applications of Laser Techniques to Fluid Mechanics, Lisbon, Portugal

Mei CC (1989) The applied dynamics of ocean surface waves. World Scientific Publishing, Singapore

Newman JN (1977) Marine Hydrodynamics. MIT Press, Cambridge, Mass

Raffel M; Willert C; Kompenhans J (1998) Particle image velocimetry. Springer, Berlin Heidelberg New York

Sveen JK (1999) An introduction to MatPIV 1.4.; Documentation and code: http: //www.math.uio.no/~jks/matpiv/

Optical Flow Systems (1999) VidPIV3 Rowan User Manual. Optical Flow Systems, Scotland

Wang J; Barnes F; Gray C (1996) A comparison between interpolation algorithms for post processing of particle image velocimetry data. Proceedings of Optical Methods in Heat and Fluid Flow, City University, UK